Evaporation Dynamics of Sessile Saline Microdroplets in Oil

Ruel Cedeno, Romain Grossier, Victoria Tishkova, Nadine Candoni, Adrian E. Flood, Stéphane Veesler

Evaporation Dynamics of Sessile Saline Microdroplets in Oil

Ruel Cedeno[a,b], Romain Grossier[a], Victoria Tishkova[a], Nadine Candoni[a], Adrian E. Flood[b]*, Stéphane Veesler[a]*

[a]CNRS, Aix-Marseille University, CINaM (Centre Interdisciplinaire de Nanosciences de Marseille), Campus de Luminy, Case 913, F-13288 Marseille Cedex 09, France

[b]Department of Chemical and Biomolecular Engineering, School of Energy Science and Engineering, Vidyasirimedhi Institute of Science and Technology, Rayong 21210, Thailand

*Email: adrian.flood@vistec.ac.th, stephane.veesler@cnrs.fr

Abstract

The occurrence of concentration and temperature gradients in saline microdroplets evaporating directly in air makes them unsuitable for nucleation studies where homogeneous composition is required. This can be addressed by immersing the droplet in oil under regulated humidity and reducing the volume to the picoliter range. However, the evaporation dynamics of such a system is not well understood. In this work, we present evaporation models applicable for arrays of sessile microdroplets with dissolved solute submerged in a thin layer of oil. Our model accounts for the variable diffusion distance due to the presence of the oil film separating the droplet and air, the variation of the solution density and water activity due to the evolving solute concentration, as well as the diffusive interaction between neighboring droplets. Our model shows excellent agreement with experimental data for both pure water and NaCl solution. With this model, we demonstrate that assuming a constant evaporation rate and neglecting the diffusive interactions can lead to severe inaccuracies in the measurement of droplet concentration particularly during nucleation experiments. Given the significance of droplet evaporation in a wide array of scientific and industrial applications, the models and insights presented herein would be of great value to many fields of interest.

INTRODUCTION

Droplet evaporation on surfaces is ubiquitous in nature and plays a key role in a wide range of industrial and scientific applications[1] such as inkjet printing[2], nanostructure fabrication[3], DNA chip manufacturing[4], crystallization studies[5], biomedical diagnostics[6], as well as virus spreading[7] and testing[8]. However, this seemingly “simple” process is governed by the complex interplay of many physical phenomena such as evaporative mass transfer[9], heat conduction and convection, thermal-hydrodynamic instabilities, viscous and inertial flows, surface-tension-driven flows, contact-line pinning and depinning, as well as buoyancy effects.[10]

Given its complexity and practical significance, numerous experimental and theoretical investigations have been devoted to better understand the underlying physics of sessile droplet evaporation[10-11] which is closely related to the physics of nanobubble dissolution.[12-13] Many of these studies dealt with the evaporation of either pure liquid droplets[14-15] or those with suspended colloidal particles which can lead to the so-called “coffee-ring effect”[16-17]. However, the evaporation of droplets containing dissolved salts has been rarely investigated. For instance, Takistov et al.[18], Shin et. al.[19], Zhang et. al.[20], and Zhong et. al.[21] showed that the resulting patterns and morphologies of the dried salt droplets depend on the wettability of the surface, i.e. crystal rings would form on hydrophilic surfaces while single crystals at the center of the droplet are likely to form on hydrophobic surfaces. This suggests that surrounding salt droplets with hydrophobic liquid is a promising approach for studying nucleation inside the droplet without interaction with the hydrophobic liquid, i.e. homogeneous primary nucleation.

In the context of crystallization studies, we need to ensure spatial homogeneity of droplet temperature and composition. However, in microliter droplets, it has been shown that various internal and Marangoni flows can lead to temperature and concentration gradients[22-23]. To address this, we reduce the droplet size down to picoliter range[24] and we reduce the evaporation rate by immersing the droplet in an oil bath. Because water can diffuse into the oil in small amounts, the oil bath is subjected to regulated humidity,[25] with the goal of controlling the diffusion of droplet water into the oil. The oil bath also serves as a thermal buffer which minimizes temperature gradients due to evaporation. To extract nucleation parameters from such experiments[26], it is crucial to determine how the volume, and so supersaturation of microdroplets, evolve with time. In modeling the evaporation rate, Soulié et. al.[27] reported that the droplet volume varies linearly with time within the early stages of evaporation. Given that the later stages of evaporation are crucial for the analysis of nucleation, we need a model that works even for the later stages. Since we are dealing with arrays of concentrated salt microdroplets immersed in a film of oil, there are additional phenomena that need to be accounted for. First, the variable diffusion distance, due to the presence of oil film separating the microdroplet and air, must be taken as an additional parameter. Second, the density of the microdroplet changes as water evaporates due to solute concentration increase. Third, the equilibrium concentration at the interface varies with time because water activity decreases as solute concentration increases (Raoult's law).[28] Fourth, the diffusive interactions due to the presence of neighboring microdroplets must be accounted for.[29] In this work, we derive expressions describing the evaporation dynamics that account for these four additional phenomena based on well-established mass transfer equations. We then validate our model with experimental data[30]. Moreover, we highlight that (1) surprisingly, different contact-line behavior such as constant contact angle (CCA), constant contact radius (CCR), and stick-slide (SS) leads to comparable evolution of microdroplet volume within the time of nucleation, and (2) failure to account for diffusive interactions between microdroplets nor the changes in colligative properties can lead to significant overestimation of their concentration. The objective of the model presented here, is to extract the supersaturation ratio at nucleation from the simultaneous observation of hundreds of microdroplets.

MODELING

When a microdroplet is deposited onto a surface, it rapidly conforms to a quasi-equilibrium geometry with contact radius R and contact angle θ, which determine the droplet volume V_d (**Figure 1**).

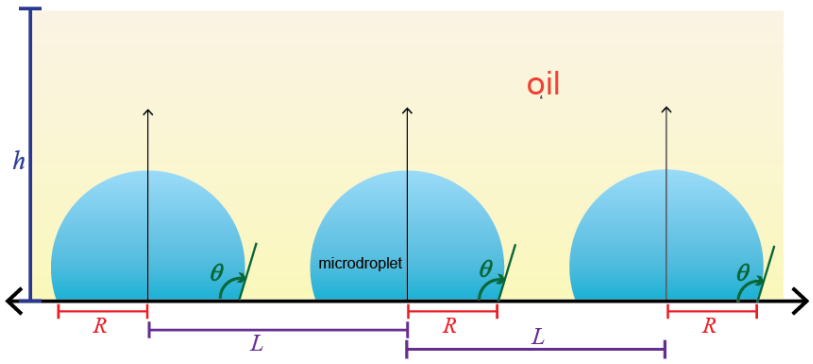

Figure 1 Geometry of the microdroplets (modeled as a spherical cap) in a linear array with contact radius R, contact angle θ immersed in oil with thickness h. The centers of neighboring microdroplets are separated by a distance L.

Contact Line Behavior of Sessile Microdroplets

As R is in the micrometer range, the droplet can be assumed to be a spherical cap (see section 1 of SI, Figure S1) due to the negligible gravitational effects (size is much less than the capillary length L_c, i.e. Bond number << 1). Thus, the droplet volume V_d can be calculated as[31]

$$V_d = \pi R^3 g(\theta) \tag{1}$$

$$g(\theta) = \frac{\sin\theta\,(\cos\theta + 2)}{3(1+\cos\theta)^2} \tag{2}$$

In the extreme case of perfectly smooth chemically homogeneous surface, the droplet maintains an equilibrium contact angle, and this is referred to as constant contact angle (CCA) mode. Consequently, during evaporation, the volume decreases due to the continuous decrease in contact radius.[31] In practice, the droplet can be pinned at some point due to surface roughness so the radius remains constant and the angle decreases due to evaporation. In the extreme case where the droplet remains pinned throughout its lifetime, we refer to this as the constant contact radius (CCR) mode. In this mode, the volume decreases due to the continuous decrease in contact angle. As experimental studies suggest,[14] real microdroplets evaporate in some mixture of CCR and CCA modes. One common observation is the occurrence of CCR mode at the beginning and once the contact angle decreases to a value less than the receding contact angle θ_r, it switches to CCA mode and the radius decreases. This combination is known as the stick-slide (SS) mode.[14, 31] In this work, we consider all three cases (CCA, CCR, and SS models) in analyzing the experimental data.

Evaporation Rate of Sessile Droplets

In the case of diffusion-limited quasi-steady state evaporation of pure liquid droplet, Popov[28] reported an analytical expression for the mass transfer rate as follows :

$$\frac{dm}{dt} = -\pi R D M_w (c_s - c_\infty) f(\theta) \tag{3}$$

$$f(\theta) = \frac{\sin\theta}{1+\cos\theta} + 4\int_0^\infty \frac{1+\cosh(2\theta\delta)}{\sin(2\pi\delta)} \tanh[(\pi-\theta)\delta]\, d\delta \tag{4}$$

where m is the mass of the volatile species (in this case, water), D is the diffusivity of water in the medium (in this case, oil), M_w is the molar mass of water, c_s and c_∞ are the concentration of water at saturation and at a point far away from the droplet respectively (in mol/m^3), $f(\theta)$ is a shape factor, and δ is an arbitrary variable of integration.

As mentioned earlier, since we are dealing with concentrated arrays of saline droplets immersed in a film of oil, there are four additional phenomena that need to be accounted for: (1) the influence of oil thickness on the evaporation rate (2) the changes in droplet density as water evaporates (3) the dependence of water activity on solute concentration, (4) the lowering of evaporation rate due to the presence of neighboring droplets.

Considering the influence of oil thickness on the evaporation rate

For a droplet submerged in an oil bath (R<<h), we assume an isothermal system so that temperature-dependent quantities such as solubility and diffusivity remain constant. The oil thickness is taken into consideration in our study by a factor *(1+R/2h)* introduced in equation (5) (see section 2.1.1 of SI), leading to:

$$\frac{dm}{dt} = -\pi R D M_w (c_s - c_\infty)\left(1 + \frac{R}{2h}\right) f(\theta) \tag{5}$$

Note that the factor *(1+R/2h)* is an *ad hoc* approximation since it was derived based on a hemispherical droplet under certain constraints (see section 2.1.1 of SI). The exact version of equation (5) should be obtained by resolving the diffusion equations in a finite domain (involving Legendre functions in toroidal coordinates[31-32]) which is beyond the scope of this study.

From equation (5), we then introduce the relative humidity *RH*, defined as water concentration divided by the concentration at saturation c_s (in this case, the solubility of water in oil). Note that technically, relative humidity is a vapor phase property (i.e. ratio of partial pressures). Since the liquid phase concentrations should scale proportionally to the partial pressures above them (Henry's Law), we can use *RH* to express the ratio of water concentrations in the liquid phase (i.e. oil) for simplicity. Then, we replace the transfer rate of *m* by the volume *V* of pure water (see section 2.1.2 of SI), leading to:

$$\frac{dV}{dt} = -\pi R K (RH_s - RH_\infty)\left(1 + \frac{R}{2h}\right) f(\theta) \tag{6}$$

Where K combines all the constant terms in $K = \frac{D M_w c_s}{\rho_w}$ with ρ_w the density of pure water, RH_s is the relative humidity at the droplet-oil interface (saturated). In the case of isolated droplets, we use the relative humidity at oil-air interface RH_∞ in equation 6.

Considering the changes in droplet density as water evaporates

To account for changes in solution density as a function of concentration, we used a linear function where ρ_w is the density of pure water, *S* is the supersaturation ratio ($S = c/c_{eq}$, where c is the concentration of salt in the solution and c_{eq} is its solubility), ρ is the density of the salt solution at *S* and b_1 is a coefficient fitted from experimental data. The experimental data used in these fittings are shown in Figure S2 of SI (see section 2.2.1 of SI).

$$\rho = \rho_w (1 + b_1 S) \tag{7}$$

Using this relation of ρ, we express the droplet volume V_d taking into account the presence of salt and water and we replace it in equation (1) to determine the droplet radius *R in terms of S* (see section 2.2.2 of SI)*:*

$$R = \left(\frac{V_d}{\pi g(\theta)}\right)^{\frac{1}{3}} = \left[\frac{V\left(1 + c_{eq} M_{\text{salt}} S\right)}{(1 + b_1 S)\pi \cdot g(\theta)}\right]^{\frac{1}{3}} \tag{8}$$

where M_{salt} is salt molar mass. Then, this expression of *R* is used in equation (6) to determine the rate of change in droplet volume.

Considering the dependence of water activity on solute concentration

To account for the lowering of water activity as concentration increases, we model the saturated relative humidity RH_s as

$$RH_s = RH_0(1 - b_2 S) \tag{9}$$

where RH_0 is the relative humidity of air that is in an equilibrium state with pure water (equal to 1), b_2 is the coefficient of vapor pressure lowering fitted from experimental data[33] (see section 2.3, Figure S3 of SI). Similarly, The use of linear approximation to fit the saturation concentration was also employed by Dunn et al.[34]

Considering the lowering of evaporation rate due to the presence of neighboring droplet

As shown in several studies,[35-36] the presence of neighboring droplets slows down the evaporation process compared to isolated sessile droplets. This is due to the diffusion-mediated interactions, which is a function of the relative spacing between the individual droplets (also known as shielding effect).[37-39] The region between neighboring droplets experiences an enhanced local accumulation of water, which in turn reduces the driving force for evaporation. In other words, each droplet experiences an effective relative humidity RH_{eff} that is higher than the far-field relative humidity RH_∞. To quantify this behavior, we adapt the result of Masoud *et al.*[40] who derived analytical expressions to describe the collective evaporation of multiple droplets applicable for any arbitrary configuration (1D or 2D array). Accordingly, if there are *N* droplets in the system, then the evaporation rate of the n^{th} droplet J_n is given by

$$\frac{J_n}{\hat{J}_n} = 1 - \sum_{\substack{m=1 \\ m \neq n}}^{N} \hat{\Phi}_{r_m} \frac{J_m}{\hat{J}_n} \tag{10}$$

where $\hat{J}_n$ is the evaporation rate of an equivalent isolated droplet, $\hat{\Phi}_{r_m}$ is the normalized vapor concentration at the location of the m^{th} droplet (any droplet other than the droplet *n*) while J_m is the evaporation rate of the m^{th} droplet. The term $\hat{\Phi}_{r_m}$ is a function of the separation distance between droplets, which takes the form

$$\hat{\Phi}_{r_m} = 4A\frac{R}{\tilde{r}} + (A - 4B)(\tilde{r}^2 - 3\tilde{z}^2)\frac{R^3}{\tilde{r}^5} + O\left[\left(\frac{R}{\tilde{r}}\right)^5\right] \tag{10a}$$

where

$$A = \int_0^\infty \left\{1 + \frac{\cosh[(2\pi - \theta)\tau]}{\cosh(\theta\tau)}\right\}^{-1} d\tau \quad , \quad B = \int_0^\infty \left\{1 + \frac{\cosh[(2\pi - \theta)\tau]}{\cosh(\theta\tau)}\right\}^{-1} \tau^2 d\tau \tag{10b}$$

in which $\tilde{r} = |r - r_c|$ and r_c is the location of the center of droplet's contact area, $\tilde{z}$ is the corresponding cartesian z-coordinate at $\tilde{r}$, θ is the contact angle, and τ is an arbitrary constant of integration.

Note that equation (10) leads to a system of *N* linear equations which gives evaporation rates for each droplet with respect to its position in the array. In a special case of long 1-D array of monodisperse microdroplets (*N* > 60), each droplet tends to evaporate at the same rate (i.e. $J_n \approx J_m$). This has been experimentally verified in our previous work.[41] With this assumption, we can simplify equation (10) as

$$\frac{J_n}{\hat{J}_n} = \left(1 + \sum_{m=1}^{N} \hat{\Phi}_{r_m}\right)^{-1} \tag{11}$$

Indeed, the predictions of the simplified model (equation 11) converges to that of the full model[40] (equation 10) at large values of *N* (see Figure S4 and section 2.4 of SI) which justifies our simplification. Furthermore, the normalized evaporate rate $J_n/\hat{J}_n$ is related to the effective relative humidity as

$$\frac{J_n}{\hat{J}_n} = \frac{RH_s - RH_{eff}}{RH_s - RH_\infty} \tag{12}$$

Thus, to describe the evaporation of microdroplet arrays, we replace RH_∞ with RH_{eff} in equation (6) which gives

$$\frac{dV}{dt} = -\pi RK\left(RH_s - RH_{eff}\right)\left(1 + \frac{R}{2h}\right) f(\theta) \tag{13}$$

Models for Contact Line Behavior

We can incorporate the contact-line behavior by modeling the behavior of the contact angle *θ*, using the time derivative of the contact angle as a function of time. The simplest case is the constant contact angle mode (CCA) in which

$$\frac{d\theta}{dt} = 0 \tag{14}$$

For constant contact radius (CCR) mode, the change in the contact angle with time can be obtained by taking the time derivative of $V = f(\theta, R)$ while treating *R* as constant (see section 1 Figure S1 of SI). This leads to (see section 3.2. of SI)

$$\frac{d\theta}{dt} = \frac{1}{V}\frac{dV}{dt}(1 + \cos\theta)^2 g(\theta) \tag{15}$$

Therefore, the time evolution of *V* and *θ* can be obtained from the numerical solution of equation (13) solved simultaneously with either equation (14) for CCA or equation (15) for CCR.

For stick-slide mode (SS), the evaporation follows CCR mode, that is, the initial contact angle θ_0 decreases until it reaches the receding contact angle θ_r where it suddenly shifts to the CCA model[31]. The full SS model can be written as (see section 3.3 of SI)

$$\frac{d\theta}{dt} = \begin{cases} \frac{1}{V}\frac{dV}{dt}(1+\cos\theta)^2 g(\theta) & \text{for } \theta_r \le \theta \le \theta_0 \\ 0 & \text{for } 0 < \theta < \theta_r \end{cases} \quad (16)$$

For the numerical solution of SS, the final condition of the CCR part is used as the initial condition of the CCA part. In contrast to the typical stick-slip mode[42], this idealized stick-slide model[31] assumes that the subsequent multiple cycles of stick and slip steps are relatively short and are considered negligible.

MATERIALS AND METHODS

To validate our models, we performed experiments using lateral view and bottom view setups. A schematic diagram of the experiment is shown in **Figure 2**.

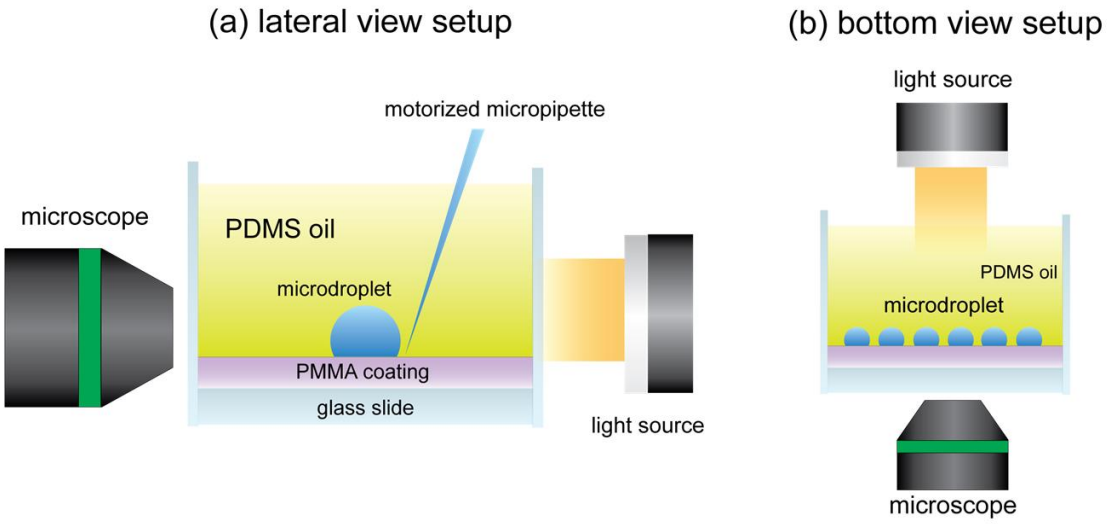

Figure 2 Schematic diagram of the experimental setup for (a) lateral view and (b) bottom-view

Using a micropipette (Femtotip Eppendorf, 0.5 µm internal diameter) attached to a motorized micromanipulator, (piezo electric, MS30 Mechonics), we generated microdroplets on the surface of a poly(methyl methacrylate) (PMMA)-coated glass slide that is immersed in PDMS oil (10 cSt, 1.5 mm-thick for lateral view and 0.8-mm thick for bottom view). The size of the oil bath was designed to be much greater than the microdroplet to avoid confinement-induced alteration of evaporation dynamics.[43] For the lateral view setup, we tracked the evolution of contact radius and droplet height from a series of lateral images of droplets acquired using a side-view microscope (Olympus BXFM equipped with Hamamatsu C11440). With simple trigonometry, the contact radius and droplet height allow calculation of contact angle and droplet volume, assuming that microdroplets are spherical caps (see section 1 of SI, Figure S1). We note that the use of side-view microscope gives direct access to geometric parameters of the microdroplets. However, it only permits measurement of 3-4 droplets at a time which is inefficient for nucleation experiments which require a large number of identical evaporating droplets in order to obtain reliable data.[44]

For the bottom-view setup, we performed a similar microdroplet generation procedure (additional details are shown in Ref[24]). Properties of products are described in Table S2 of SI (see section 4.1 of SI). We used an approach based on the analysis of gray-level pixel standard deviation[26] of

axial-view droplet images (see section 5.2 of SI, Figure S7). We measured three characteristic times namely the saturation time (droplet is saturated), matching time (refractive index of droplet equals that of the oil), and nucleation time. Although the use of the bottom-view microscope only gives the droplet volume and concentration at some specific time points, it allows simultaneous measurement of hundreds of droplets, which is useful for studying the stochastic nature of nucleation.[41]

Moreover, we measured the solubility and diffusivity of water in PDMS oil (10 cSt) using Karl-Fischer titration and droplet evaporation method respectively. The details are shown in sections 4.2 and 4.3 of SI.

RESULTS AND DISCUSSION

Predictions of three models (CCR, CCA, and SS) for Isolated Pure Droplet

First, we considered the case of isolated pure water droplet. **Figure 3a** shows the droplet images at selected time points while the corresponding geometric parameters are plotted in **Figure 3b-e** along with the predictions of three models (CCR, CCA, and SS). The experimental points in **Figure 3b** suggests that the normalized contact radius R/R_0 is constant until a certain time of pinning t_p, after which, R/R_0 decreases. Meanwhile, **Figure 3**c shows that the contact angle θ decreases until this threshold at t_p and then remains relatively constant. This behavior indicates that the system undergoes a stick-slide (SS) mode, i.e. CCR followed by CCA. In our system, we found that the time of pinning t_p corresponds to a contact angle of around 97° (**Figure 3**c). Thus we assume a receding contact angle of θ_r=97° and we use this value for the stick-slide (SS) model in equation (16). Upon comparing the experimental points with the model predictions, it is clear that the stick-slide (SS) model well captures the evolution of the microdroplet geometric parameters (i.e. contact angle, contact radius, height, and volume). Note that the CCR period appears to be relatively shorter compared to CCA, which can be attributed to the smooth surface of PMMA-coated glass. Interestingly, regardless of the contact-line behavior (CCR, CCA, SS), the droplet volume evolves almost identically (**Figure 3**e). This is in agreement with Stauber et. al.[15] who showed that for contact angles $90^o<\theta<180^o$, the volume evolution of the two extreme modes CCA and CCR tend to converge.

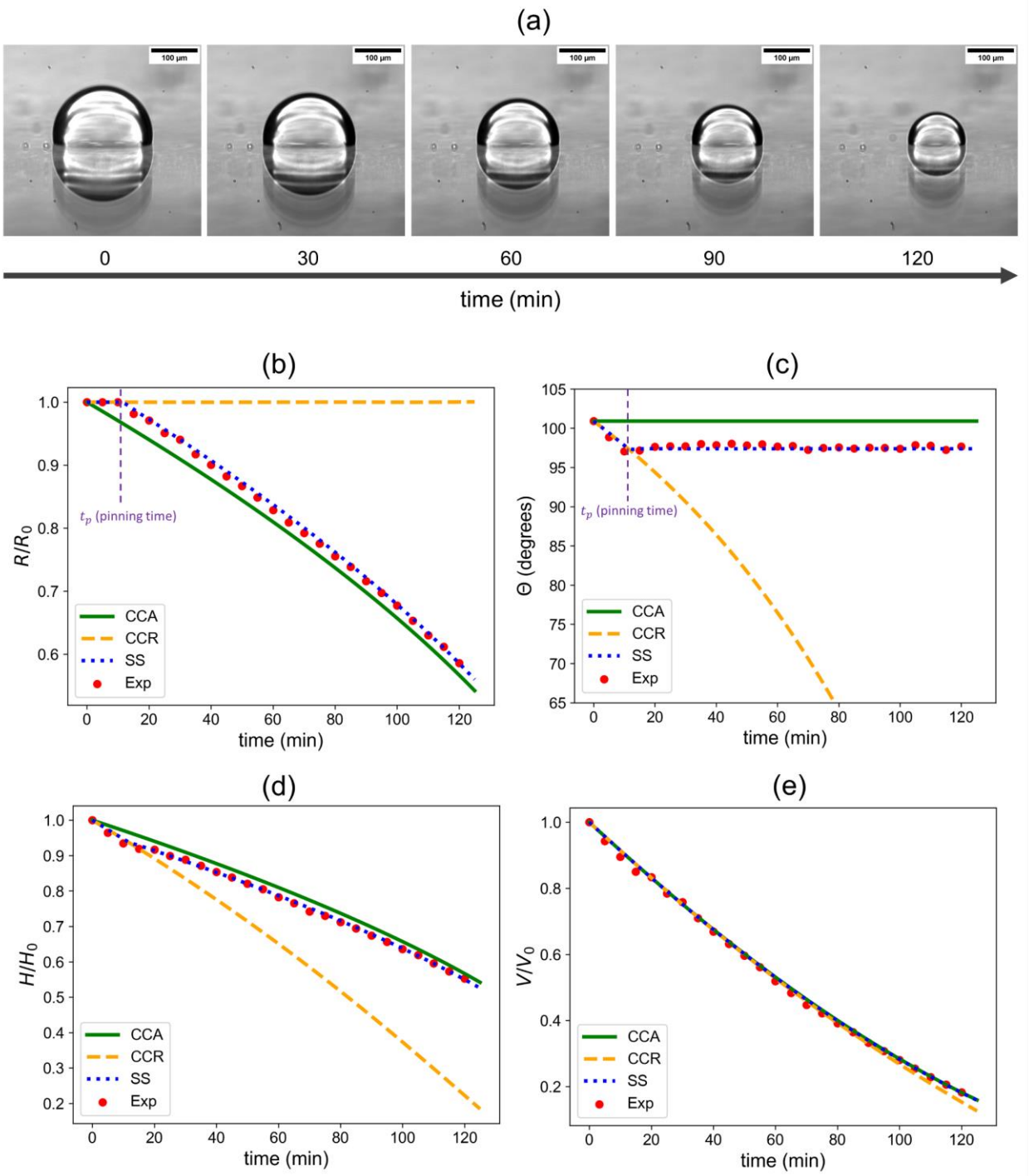

Figure 3 (a) Lateral image of pure water droplets (V_0=3.4 nL, RH=0.45) at selected time points (b) model predictions of three contact line behavior models (CCR, CCA, SS) in comparison with experimental data in terms of normalized contact radius, (c) contact angle of the microdroplets with the substrate (d) normalized microdroplet height and (e) Volume contraction.

To visualize the evolution of droplet shape, we used the numerical solution in **Figure 4** to simulate the geometry of the droplet at discrete time points. In **Figure 4**, we see that the final droplet shape is highly dependent on the contact-line behavior.

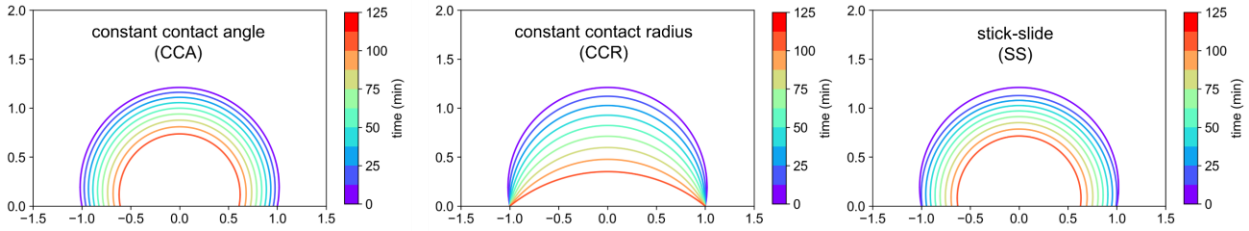

Figure 4 Predicted evolution of microdroplet shape (pure water) for CCR, CCA, and SS models at discrete time points. X, Y axis (lengths) are in terms of R/R_0.

Note that for the prediction of geometric parameters (R/R_0, θ, H/H_0), the SS model is the most suitable as illustrated in **Figure 3**. However, in the context of crystallization studies, the most important parameter to obtain from the evaporation modeling is the evolution of droplet volume on which the solution concentration depends. Thus, regardless of the droplet shape, the convergence of CCR, CCA, and SS in terms of droplet volume (**Figure 3e**) indicates that we can just choose one of these three contact-line behavior models to calculate the droplet concentration without sacrificing accuracy. Consequently, we use CCA (equation 14) to describe the evaporation rate (equation 13) in the subsequent calculations for simplicity.

CCA Model Predictions for Isolated Saline Microdroplet

Using the CCA model, we extend our analysis to isolated microdroplet containing dissolved salt (NaCl). Snapshots at 30 min interval are shown in **Figure 5a** and the results are plotted in **Figure 5b-c** along with the model predictions.

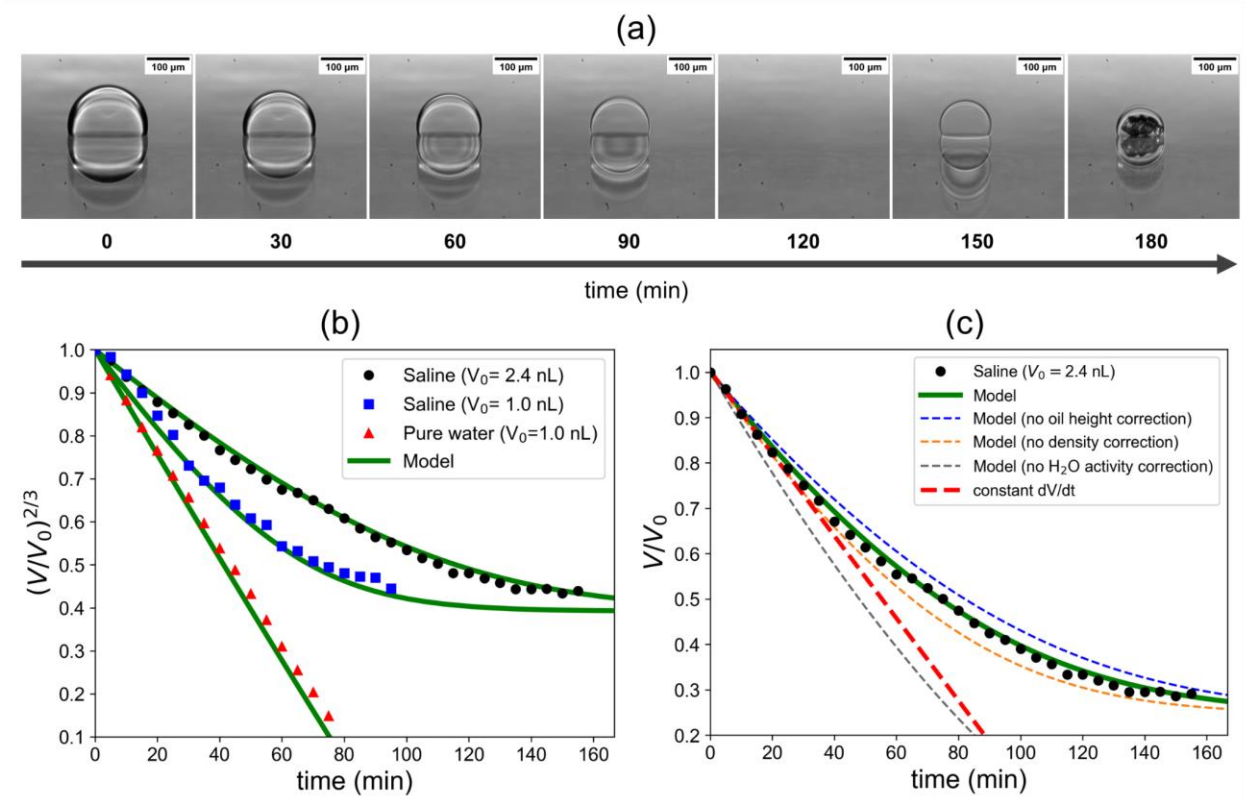

Figure 5 (a) Lateral images of isolated saline droplet for V_0 = 2.4 nL, S_0 = 0.6, *RH*=0.45 at selected time points. At 120 min, the droplet optically disappears due to refractive index matching of the saline microdroplet and PDMS oil (b) Model predictions for the time evolution of $(V/V_0)^{2/3}$ for saline (2.4 nL, 1.0 nL) and pure water droplet (1.0 nL) (c) Model predictions for the time evolution of (V/V_0) under different assumptions.

For pure liquid droplets, Picknett and Bexon[14] have shown that the plot of $V^{2/3}$ must be linear with time (see Section 4.3. of SI). This is also known as the d^2-law[45] (since $V^{2/3} \propto d^2$). However, **Figure 5b** shows that for droplets containing dissolved salts, this rule is no longer applicable as the evaporation rate slows down with time. Meanwhile, our CCA model is able to capture this departure from linearity with excellent accuracy. Recall that in our model derivation, we incorporated modifications in order to account for the presence of salt and oil medium. Thus, it would be interesting to see how each model modification affect the model predictions. In **Figure 5c**, we see that neglecting the oil height correction can slightly overestimate the predicted volume. This is because without the oil height parameter, the droplet is considered to evaporate in an infinite medium of oil thereby hindering evaporation. Without density correction, the evaporation rate is overestimated because the volume occupied by the NaCl in the droplet is not accounted which then affects the surface area to volume ratio. Remarkably, failure to correct for the changes in water activity due to the presence of salt (Raoult's law) led to a drastic overestimation of evaporation rate. The linear decrease of droplet volume when neglecting changes in water activity is consistent with what is observed in pure droplets. To verify whether the saline droplets have a homogeneous composition throughout the evaporation process, we plotted the Peclet number as a function of time (see Section 5.1. of SI and Figure S6) and we found that the maximum *Pe* is in the order of 10^{-4} suggesting a uniform droplet concentration.

CCA Model Predictions for Microdroplet Arrays

Having validated our models on isolated microdroplets, we then extend our analysis to arrays of multiple droplets. First, we consider the case of long 1-D array of monodisperse pure water droplets (N > 60). Exemplary images are presented in **Figure 6a** which shows 4 droplets within the field of view. The corresponding evolution of droplet volume is plotted in **Figure 6b** which demonstrates that the presence of neighboring droplets indeed slow down the evaporation rate in comparison with isolated droplets (shielding effect).

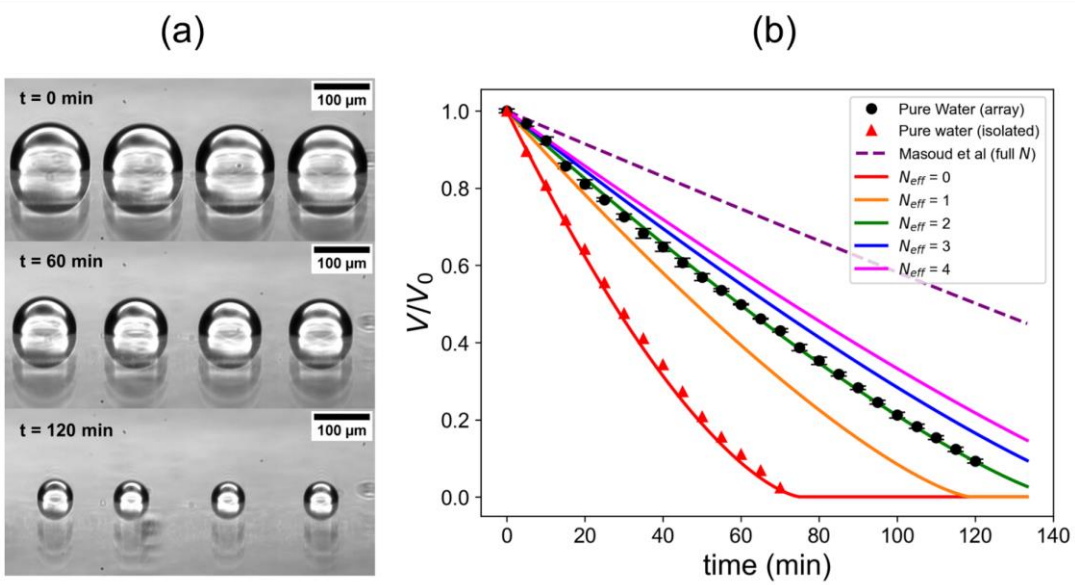

Figure 6 (a) Exemplary lateral images of pure microdroplet arrays (V_0 = 1.0 nL, L/R_0 = 2.5, RH = 0.40) (b) model predictions in terms of droplet volume in comparison with experimental data. The error bars represent the standard deviation of 4 droplets.

To model this behavior, we employ the work of Masoud et al[40]. Briefly, if there are N droplets in the system, then the reduction of evaporation rate of each droplet is a function of the sum of the contributions of all the other droplets (equation 10). However, if we use Masoud's full model (considering the presence of all 60 neighbors), the evaporation rate is significantly underestimated (dashed curve in **Figure 6b**). We hypothesize that due to the presence of oil, each droplet could not entirely "feel" the presence of all other droplets, but only that of its close adjacent neighbors ("insulating effect"). To determine how many adjacent neighbors effectively contribute to the local relative humidity (we denote as N_{eff}), we tested several values of N_{eff} (**Figure 6b**). When N_{eff} is set to zero, the model is reduced to the case of isolated droplet. When N_{eff} = 1 (i.e., 1 neighbor to the left and 1 to the right), the evaporation rate is overestimated. When N_{eff} = *2,* the model accurately predicts the evaporation behavior whereas N_{eff} >2 underestimates the rate. This empirical evidence suggests that there are two adjacent droplets from both sides that effectively contribute to the local humidity condition. To further verify this, we performed experiments on saline microdroplet arrays. Exemplary images are shown in **Figure 7a** (videos in SI) and the results are plotted in **Figure 7b**. Indeed, with N_{eff}=2, our model accurately predicts the evaporation behavior across different volumes and separation distances.

To highlight the importance of our model modifications, we compare the complete model against that in which one consideration is removed (for V_0= 340 pL). The results in terms of normalized volume and supersaturation ratio are shown in **Figure 7c** and **Figure 7d**, respectively. As in the case of isolated saline droplet, the impact of density changes and oil height correction is less important compared to water activity changes. Interestingly, neglecting the "shielding effect" of the neighboring droplets would result in more severe inaccuracies. Such errors will have a large impact on the predicted droplet concentration (**Figure 7d**).

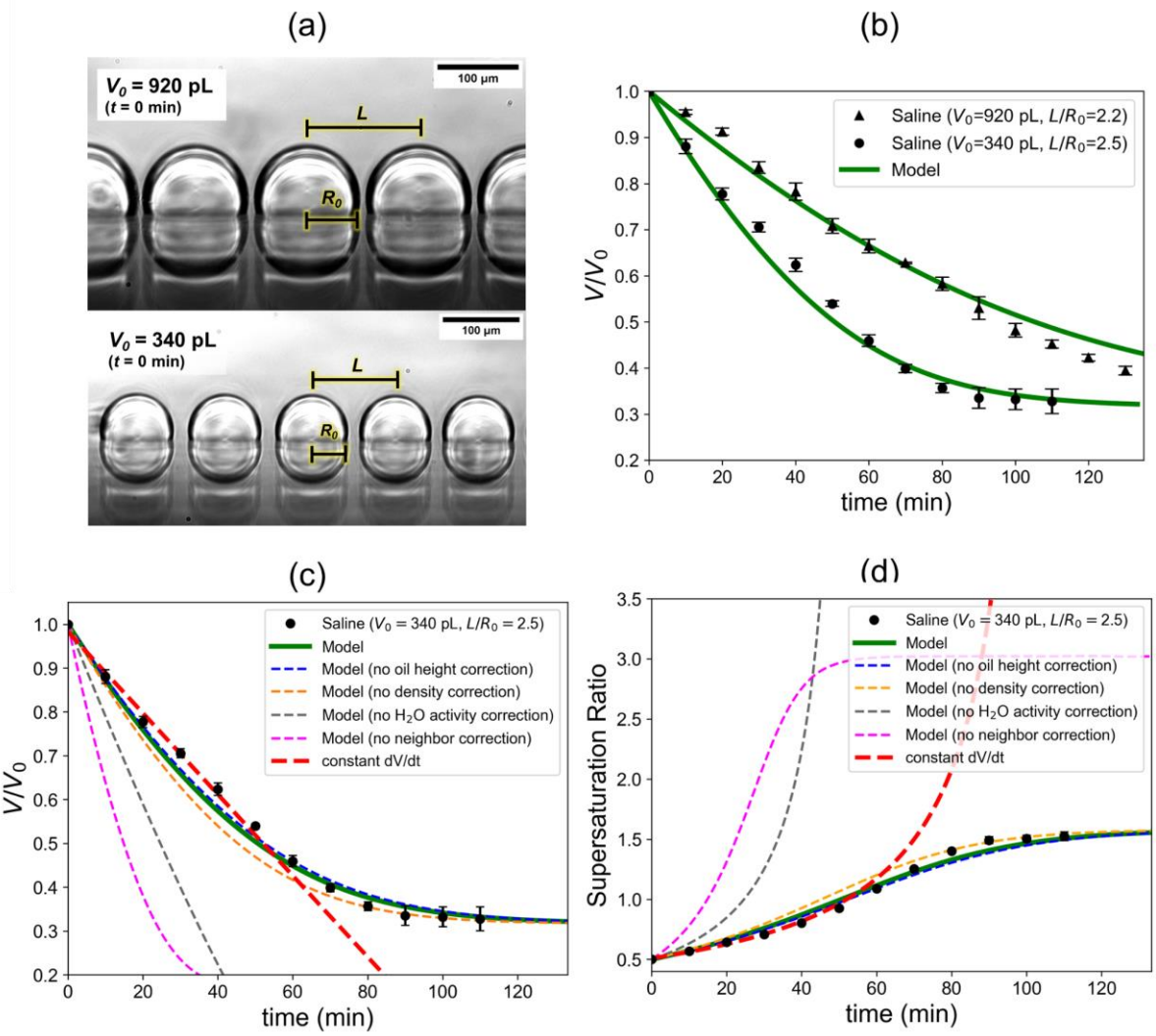

Figure 7 (a) Lateral images of saline microdroplet arrays (S_0 = 0.60, RH = 0.32) with different initial volume and separation distance (b) model predictions in terms of droplet volume in comparison with experimental data (c) comparison of model predictions for V_0 = 340 pL in terms of normalized volume and (d) in terms of supersaturation ratio.

Application to Nucleation Experiments

Having experimentally validated our model for microdroplet arrays, we then explore its application to nucleation studies. Due to the stochastic nature of nucleation, large number of independent induction times measurements is necessary to quantify its kinetics. To address this, we have

recently developed a method to measure induction times of hundreds of sessile microdroplets based on images taken from a bottom-view microscope.[41] A schematic diagram of a typical microdroplet configuration (2D matrix) is shown in **Figure 8a** and an example image is shown in **Figure 8b** where the distance between droplet lines is always much greater than the distance between adjacent droplets (i.e. $L_2 > L_1$). To minimize the "edge effects", (i.e. outermost lines evaporate faster than the middle lines), we add more lines above and below so that the lines inside the field of view are of essentially uniform hygrometric environment.

Our setup allows us to measure two experimental points shown in **Figure 8c**. The first point corresponds to the time at which the solution in the microdroplet is saturated (S=1), and the second point is the time at which the refractive index of the microdroplet matches that of the oil (S=1.395). To model the shielding effect in this 2D matrix, we employ the same arguments as in the 1D-case (using N_{eff} = 2) with the additional assumption that each line is influenced by its direct adjacent line (i.e. 1 line above and 1 line below). Applying this, we obtain excellent agreement with experimental data across multiple sizes, initial concentrations, and separation distances. This further validates the wide applicability of our model.

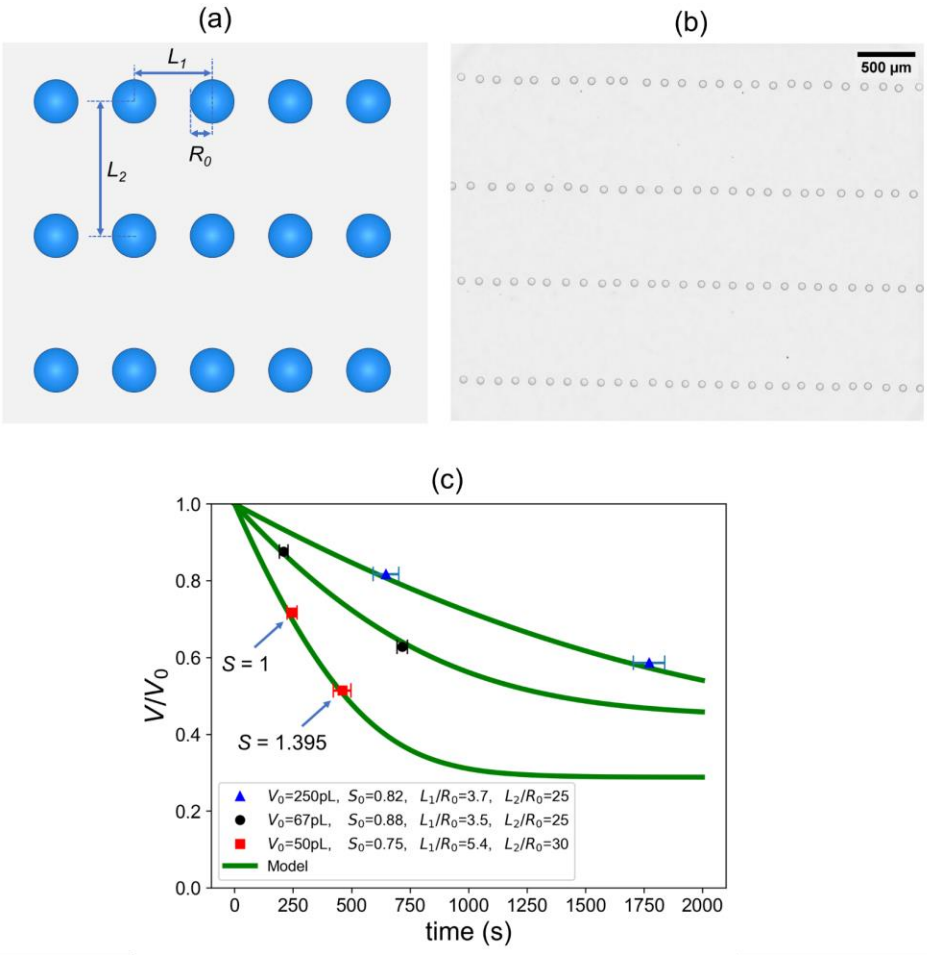

Figure 8 (a) Schematic diagram of 2D-array of monodisperse microdroplets (b) Exemplary bottom-view images of saline microdroplet arrays (c) model predictions in terms of droplet volume in comparison with experimental data (all at RH = 0.10). The error bars at saturation time (S=1) and matching time (S=1.395) represent the standard errors taken from the measurement of hundreds of microdroplets.

In a typical nucleation experiment involving bottom-view images, the time of nucleation (induction time) can be readily obtained (see Section 5.2. of SI), however, the concentration of each microdroplet during the onset of nucleation is not directly accessible. In principle, if we know the supersaturation ratio at nucleation S_n, the distribution of induction times can be used to estimate the important nucleation kinetic parameters. Here, we show that our evaporation model would be useful for this purpose.

In the absence of a suitable evaporation model, several reports assumed a constant evaporation rate to calculate the droplet concentration as a function of time for nucleation kinetic measurements[46-48]. Here, we highlight that this approximation can lead to inaccurate values of droplet concentration particularly in later stages where nucleation occurs. To illustrate this, we compare the predictions of our complete CCA model against that of constant *dV/dt* approximation in **Figure 9** in terms of volume and supersaturation ratio.

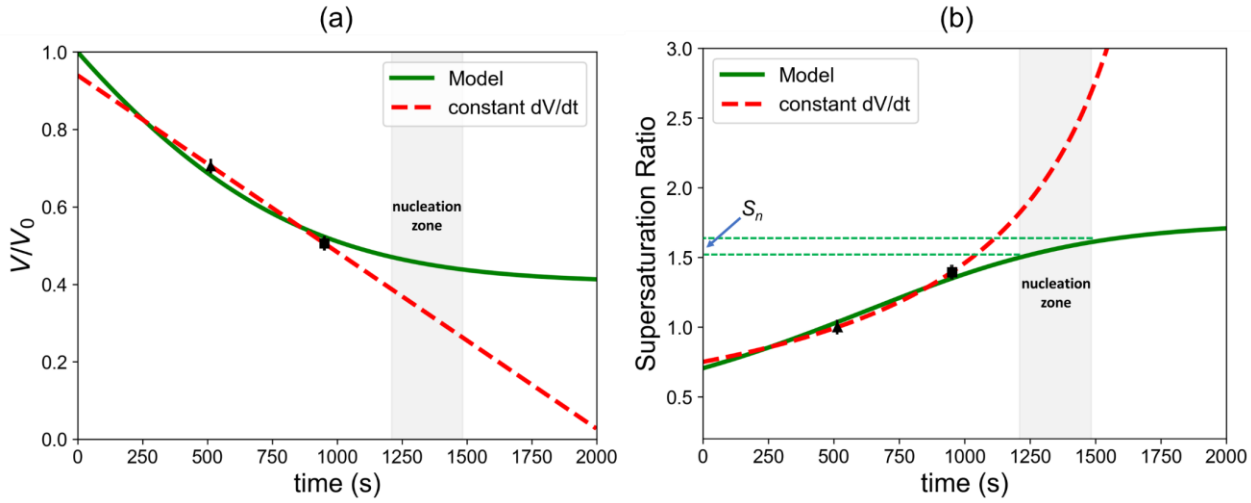

Figure 9 Model predictions (CCA) for saline microdroplets (V_0 = 55 pL, S_0 = 0.70, *RH* = 0.35, $\hat{L}_1$=5.6, $\hat{L}_2$=32) in terms of (a) droplet volume and (b) supersaturation ratio in comparison with experimental data. The error bars at saturation time (S=1) and matching time (S=1.395) represent the standard errors taken from the measurement of 90 microdroplets.

Using our model, the supersaturation at nucleation S_n ranges from S = 1.5 to 1.6 **(Figure 9b)**. This is consistent with the results of Desarnaud et. al.[49] who showed a metastability limit of at least *S* = 1.60 for NaCl-water system using microcapillary experiments. However, if we assume a constant evaporation rate by extrapolating *t* = saturation time and *t* = matching time, the predicted range of S_n would be grossly overestimated. This discrepancy would have a huge consequence particularly in crystallization studies. To illustrate this, we plot the cumulative probability distribution as a function of supersaturation at nucleation S_n in **Figure 10**.

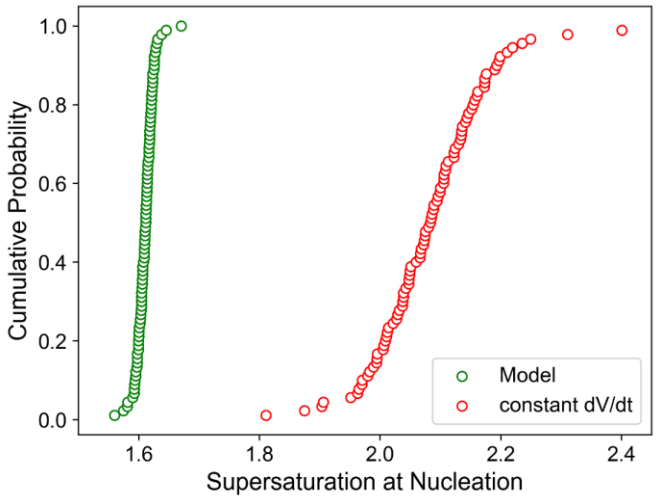

Figure 10 Cumulative probability distribution of supersaturation ratio at nucleation S_n based on two evaporation models for the experimental condition described in Figure 9.

The constant evaporation rate assumption clearly overestimates S_n resulting in significantly larger values of supersaturation. Moreover, such errors are particularly problematic for experiments conducted in ambient relative humidity (see Section 6 of SI, Figure S8). Thus, we highlight the need for accurate modeling of evaporation rate of sessile droplets in the context of nucleation studies.

CONCLUSION

In this work, we studied the evaporation dynamics of sessile saline picoliter droplets in oil until crystallization. Starting from well-established mass transfer equations for pure sessile droplets evaporating in air, we derived new expressions applicable for droplets with dissolved solute submerged in a thin layer of oil. Our model accounts for the additional complexity due to (i) variable diffusion distance due to the presence of oil (ii) density change as concentration increases (iii) water activity change as a function of concentration (iv) diffusive interactions due to the presence of neighboring droplets. By comparing our model predictions to experimental data, we showed that different contact-line behavior (CCR, CCA, or SS) results in almost identical evolution of droplet volume especially within the time scale relevant to crystallization studies. With this information, we analyzed the evaporation rate of saline droplets using the CCA model and using NaCl-water as a model system. We demonstrated for the first time that assuming a constant evaporation rate as well as neglecting the diffusive interactions between droplets can lead to severe discrepancies in the measurement of droplet concentration particularly during nucleation. This indicates that crystallization studies in literature that had used this assumption may be subject to large errors. With our model, we can accurately determine the time evolution of droplet concentration which is important in quantifying crystallization kinetics. Moreover, given the importance of evaporation dynamics in a wide array of scientific and practical applications, our models and new insights presented herein would be of great value to many fields of interest.

ACKNOWLEDGEMENTS

R. Cedeno acknowledges the financial support of Vidyasirimedhi Institute of Science and Technology (VISTEC) and the Eiffel Excellence Scholarship (N°P744524E) granted by the French Government. The authors acknowledge Virginie Heran for the assistance with Karl-Fischer titration.

SUPPORTING INFORMATION

Contact Line Behavior of Sessile Microdroplets
Evaporation Rate of Sessile Droplets
Models for Contact Line Behavior
Parameters and properties
Measurement in Saline Microdroplets
Effect of Relative Humidity on the Predicted Supersaturation at Nucleation

Videos of saline microdroplet arrays of 340 and 920pL.

This information is available free of charge via the Internet at http://pubs.acs.org/

ORCID

Ruel Cedeno: 0000-0001-9948-3943
Romain Grossier: 0000-0002-5207-2087
Victoria Tishkova 0000-0003-0283-3498
Nadine Candoni: 0000-0002-7916-7924
Adrian Flood: 0000-0003-1691-3085
Stéphane Veesler: 0000-0001-8362-2531

REFERENCES

1. Zang, D.; Tarafdar, S.; Tarasevich, Y. Y.; Dutta Choudhury, M.; Dutta, T., Evaporation of a Droplet: From physics to applications. *Phys. Rep.* **2019,** *804*, 1-56.
2. Yoo, H.; Kim, C., Experimental studies on formation, spreading and drying of inkjet drop of colloidal suspensions. *Colloids Surf., A* **2015,** *468*, 234.
3. Chen, J.; Liao, W.-S.; Chen, X.; Yang, T.; Wark, S. E.; Son, D. H.; Batteas, J. D.; Cremer, P. S., Evaporation-Induced Assembly of Quantum Dots into Nanorings. *ACS Nano* **2009,** *3* (1), 173-180.
4. Dugas, V.; Broutin, J.; Souteyrand, E., Droplet evaporation study applied to DNA chip manufacturing. *Langmuir* **2005,** *21*, 9130.
5. Hammadi, Z.; Candoni, N.; Grossier, R.; Ildefonso, M.; Morin, R.; Veesler, S., Small-volume nucleation. *C. R. Phys.* **2013,** *14*, 192.
6. Sefiane, K., On the Formation of Regular Patterns from Drying Droplets and Their Potential Use for Bio-Medical Applications. *Journal of Bionic Engineering* **2010,** *7*, S82-S93.
7. Bhardwaj, R.; Agrawal, A., Likelihood of survival of coronavirus in a respiratory droplet deposited on a solid surface. *Physics of Fluids* **2020,** *32* (6), 061704.
8. Zhang, J.; Mahalanabis, M.; Liu, L.; Chang, J.; Pollock, N.; Klapperich, C., A disposable microfluidic virus concentration device based on evaporation and interfacial tension. *Diagnostics* **2013,** *3*, 155.
9. Semenov, S.; Starov, V. M.; Velarde, M. G.; Rubio, R. G., Droplets evaporation: Problems and solutions. *The European Physical Journal Special Topics* **2011,** *197* (1), 265.
10. Larson, R. G., Transport and deposition patterns in drying sessile droplets. *AlChE J.* **2014,** *60* (5), 1538-1571.
11. Wilson, S. K.; Duffy, B. R., Chapter 4 Mathematical Models for the Evaporation of Sessile Droplets. In *Drying of Complex Fluid Drops: Fundamentals and Applications*, The Royal Society of Chemistry: 2022; pp 47-67.
12. Lohse, D.; Zhang, X., Surface nanobubbles and nanodroplets. *Reviews of Modern Physics* **2015,** *87* (3), 981-1035.
13. Liu, Y.; Zhang, X., A review of recent theoretical and computational studies on pinned surface nanobubbles. *Chinese Physics B* **2018,** *27* (1), 014401.
14. Picknett, R. G.; Bexon, R., The evaporation of sessile or pendant drops in still air. *J. Colloid Interface Sci.* **1977,** *61*, 336.
15. Stauber, J. M.; Wilson, S. K.; Duffy, B. R.; Sefiane, K., Evaporation of droplets on strongly hydrophobic substrates. *Langmuir* **2015,** *31*, 3653.
16. Deegan, R. D.; Bakajin, O.; Dupont, T. F.; Huber, G.; Nagel, S. R.; Witten, T. A., Capillary flow as the cause of ring stains from dried liquid drops. *Nature* **1997,** *389*, 827.
17. Li, Y.; Diddens, C.; Segers, T.; Wijshoff, H.; Versluis, M.; Lohse, D., Evaporating droplets on oil-wetted surfaces: Suppression of the coffee-stain effect. *Proceedings of the National Academy of Sciences* **2020,** *117* (29), 16756-16763.
18. Takhistov, P.; Chang, H., Complex Stain Morphologies. *Ind. Eng. Chem. Res.* **2002,** *41*, 6256.
19. Shin, B.; Moon, M. W.; Kim, H. Y., Rings, Igloos, and Pebbles of Salt Formed by Drying Saline Drops. *Langmuir* **2014,** *30*, 12837.
20. Zhang, J.; Borg, M. K.; Sefiane, K.; Reese, J. M., Wetting and evaporation of salt-water nanodroplets: A molecular dynamics investigation. *Physical Review E* **2015,** *92* (5), 052403.
21. Zhong, X.; Ren, J.; Duan, F., Wettability Effect on Evaporation Dynamics and Crystalline Patterns of Sessile Saline Droplets. *The Journal of Physical Chemistry B* **2017,** *121* (33), 7924-7933.
22. Hu, H.; Larson, R. G., Analysis of the Effects of Marangoni Stresses on the Microflow in an Evaporating Sessile Droplet. *Langmuir* **2005,** *21* (9), 3972-3980.

23. Efstratiou, M.; Christy, J.; Sefiane, K., Crystallization-Driven Flows within Evaporating Aqueous Saline Droplets. *Langmuir* **2020,** *36* (18), 4995-5002.
24. Grossier, R.; Hammadi, Z.; Morin, R.; Magnaldo, A.; Veesler, S., Generating nanoliter to femtoliter microdroplets with ease. *Appl. Phys. Lett.* **2011,** *98* (9), 091916.
25. Cedeno, R.; Grossier, R.; Lagaize, M.; Nerini, D.; Candoni, N.; Flood, A. E.; Veesler, S., Nucleation in Sessile Saline Microdroplets: Induction Time Measurement via Deliquescence-Recrystallization Cycling *Faraday Discuss.* **2022,** *235*, 183-197.
26. Grossier, R.; Tishkova, V.; Morin, R.; Veesler, S., A parameter to probe microdroplet dynamics and crystal nucleation. *AIP Advances* **2018,** *8* (7), 075324.
27. Soulié, V.; Karpitschka, S.; Lequien, F.; Prené, P.; Zemb, T.; Moehwald, H.; Riegler, H., The evaporation behavior of sessile droplets from aqueous saline solutions. *PCCP* **2015,** *17* (34), 22296-22303.
28. Popov, Y. O., Evaporative deposition patterns: Spatial dimensions of the deposit. *Physical Review E* **2005,** *71* (3), 036313.
29. Hatte, S.; Pandey, K.; Pandey, K.; Chakraborty, S.; Basu, S., Universal evaporation dynamics of ordered arrays of sessile droplets. *J. Fluid Mech.* **2019,** *866*, 61-81.
30. Rodríguez-Ruiz, I.; Hammadi, Z.; Grossier, R.; Gómez-Morales, J.; Veesler, S., Monitoring Picoliter Sessile Microdroplet Dynamics Shows That Size Does Not Matter. *Langmuir* **2013,** *29* (41), 12628-12632.
31. Stauber, J. M.; Wilson, S. K.; Duffy, B. R.; Sefiane, K., On the lifetimes of evaporating droplets with related initial and receding contact angles. *Physics of Fluids* **2015,** *27* (12), 122101.
32. Nguyen, T. a. H.; Nguyen, A. V., On the lifetime of evaporating sessile droplets. *Langmuir* **2012,** *28*, 1924.
33. An, D. T.; Teng, T. T.; Sangster, J. M., Vapour pressures of CaCl2–NaCl–H2O and MgCl2–NaCl–H2O at 25 °C. Prediction of the water activity of supersaturated NaCl solutions. *Can. J. Chem.* **1978,** *56* (14), 1853-1855.
34. Dunn, G. J.; Wilson, S. K.; Duffy, B. R.; David, S.; Sefiane, K., The strong influence of substrate conductivity on droplet evaporation. *J. Fluid Mech.* **2009,** *623*, 329.
35. Carrier, O.; Shahidzadeh-Bonn, N.; Zargar, R.; Aytouna, M.; Habibi, M.; Eggers, J.; Bonn, D., Evaporation of water: evaporation rate and collective effects. *J. Fluid Mech.* **2016,** *798*, 774-786.
36. Laghezza, G.; Dietrich, E.; Yeomans, J. M.; Ledesma-Aguilar, R.; Kooij, E. S.; Zandvliet, H. J. W.; Lohse, D., Collective and convective effects compete in patterns of dissolving surface droplets. *Soft Matter* **2016,** *12* (26), 5787-5796.
37. Fairhurst, D. J., Predicting evaporation rates of droplet arrays. *J. Fluid Mech.* **2022,** *934*, F1.
38. Wray, A. W.; Wray, P. S.; Duffy, B. R.; Wilson, S. K., Contact-line deposits from multiple evaporating droplets. *Physical Review Fluids* **2021,** *6* (7), 073604.
39. Wray, A. W.; Duffy, B. R.; Wilson, S. K., Competitive evaporation of multiple sessile droplets. *J. Fluid Mech.* **2019,** *884*, A45.
40. Masoud, H.; Howell, P. D.; Stone, H. A., Evaporation of multiple droplets. *J. Fluid Mech.* **2021,** *927*, R4.
41. Cedeno, R.; Grossier, R.; Lagaize, M.; Nerini, D.; Candoni, N.; Flood, A.; Veesler, S., Nucleation in sessile saline microdroplets: induction time measurement via deliquescence–recrystallization cycling. *Faraday Discuss.* **2022,** *235* (0), 183-197.
42. Orejon, D.; Sefiane, K.; Shanahan, M. E. R., Stick–Slip of Evaporating Droplets: Substrate Hydrophobicity and Nanoparticle Concentration. *Langmuir* **2011,** *27* (21), 12834-12843.
43. Bansal, L.; Chakraborty, S.; Basu, S., Confinement-induced alterations in the evaporation dynamics of sessile droplets. *Soft Matter* **2017,** *13* (5), 969-977.
44. Hammadi, Z.; Grossier, R.; Zhang, S.; Ikni, A.; Candoni, N.; Morin, R.; Veesler, S., Localizing and inducing primary nucleation. *Faraday Discuss.* **2015,** *179* (0), 489-501.

45. Barba, F. D.; J.Wang; Picano, F., Revisiting D 2-law for the evaporation of dilute droplets. *Physics of Fluids* **2021,** *33* (5), 051701.
46. Bhamidi, V.; Kenis, P. J. A.; Zukoski, C. F., Probability of Nucleation in a Metastable Zone: Induction Supersaturation and Implications. *Cryst. Growth Des.* **2017,** *17*, 1132.
47. Talreja, S.; Kim, D. Y.; Mirarefi, A. Y.; Zukoski, C. F.; Kenis, P. J. A., Screening and optimization of protein crystallization conditions through gradual evaporation using a novel crystallization platform. *J. Appl. Crystallogr.* **2005,** *38* (6), 988-995.
48. Bhamidi, V.; Varanasi, S.; Schall, C. A., Measurement and Modelling of Protein Crystal Nucleation Kinetics. *Cryst. Growth Des.* **2002,** *2*, 395.
49. Desarnaud, J.; Derluyn, H.; Carmeliet, J.; Bonn, D.; Shahidzadeh, N., Metastability Limit for the Nucleation of NaCl Crystals in Confinement. *The Journal of Physical Chemistry Letters* **2014,** *5* (5), 890-895.

TOC graphic

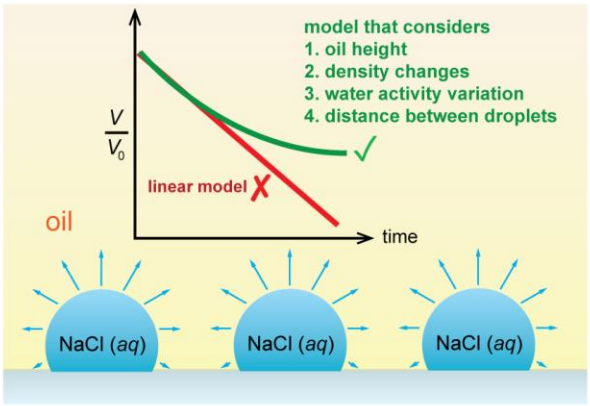
model that considers
1. oil height
2. density changes
3. water activity variation
4. distance between droplets
V
V0
linear model
oil
time
NaCl (aq)
NaCl (aq)
NaCl (aq)

Supporting Information for:

Evaporation Dynamics of Sessile Saline Microdroplets in Oil

Ruel Cedeno[a,b], Romain Grossier[a], Victoria Tishkova[a], Nadine Candoni[a], Adrian E. Flood[b]*, Stéphane Veesler[a]*

[a]CNRS, Aix-Marseille University, CINaM (Centre Interdisciplinaire de Nanosciences de Marseille), Campus de Luminy, Case 913, F-13288 Marseille Cedex 09, France

[b]Department of Chemical and Biomolecular Engineering, School of Energy Science and Engineering, Vidyasirimedhi Institute of Science and Technology, Rayong 21210, Thailand

1. Contact Line Behavior of Sessile Microdroplets

When a droplet is deposited onto a surface, it rapidly conforms to a quasi-equilibrium geometry with contact radius R, and contact angle θ, which determine the droplet volume V_d. The shape of the droplet is either spherical or flattened, depending on the value of R compared to the capillary length L_c which characterizes the ratio of the interfacial energy between the droplet and the medium $\gamma_{(droplet/medium)}$ to gravitational effects. L_c can be calculated as

$$L_c = \sqrt{\frac{\gamma_{(\mathrm{droplet}/medium)}}{\Delta\rho \times g}} \qquad \text{(S1)}$$

where $\Delta\rho$ is the density difference between the solution and the surrounding medium and g is the gravitational acceleration. In our case, the droplet is either pure water or saline solution and the medium is PDMS oil. If the droplet size is much less than L_c, then the droplet assumes a spherical cap geometry. For the PDMS-water system[1], the capillary length is in the millimeter range. Since R is in the micrometer range, (much smaller than L_c), the gravity effect is negligible compared to the interfacial effect between droplet and oil and so the droplets can be assumed to be a spherical cap. Thus, the droplet volume V_d can be calculated as[2]

$$V_d = \pi R^3 g(\theta) \text{ with } g(\theta) = \frac{\sin\theta(\cos\theta+2)}{3(1+\cos\theta)^2} \qquad \text{(S2)}$$

In the following section, we derive expressions for the diffusion-controlled evaporation of saline microdroplet with contact radius R and constant contact angle θ immersed in a PDMS oil bath with thickness h. The different cases (θ>90°, θ=90°, θ<90°) are shown in **Figure S1**. Recall that we define r as the radial distance from the center of the equivalent

spherical cap at an angle of ϕ with the equatorial line.

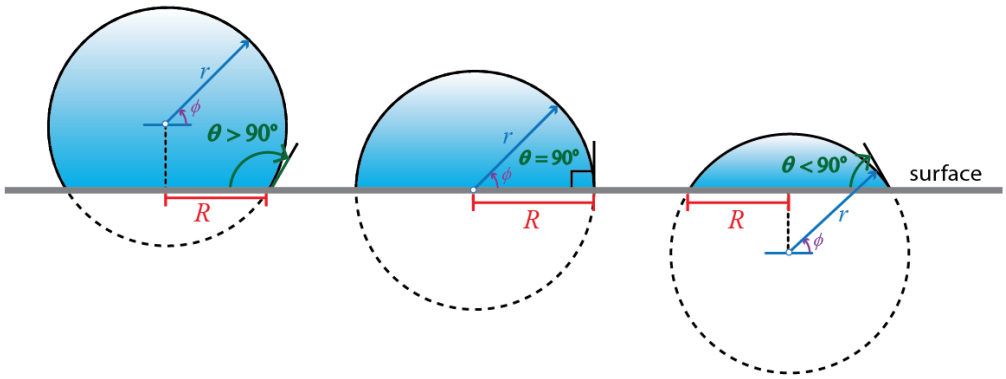

Figure S1. Illustration of microdroplet showing the equivalent spherical cap at different values of contact angle θ.

For simplicity, we will first consider the case where θ=90° (hemispherical droplet) which exhibits uniform evaporation flux over the surface area. Later on, we will incorporate a widely-used shape factor[3-4] denoted as $f(\theta)$ to obtain a general expression for any value of θ.

2. Evaporation Rate of Sessile Droplets

2.1 Influence of oil thickness on the evaporation rate

2.1.1. Introduction of the factor (1+R/2h) (leading to equation 5 in the main text)

Since the microdroplet is submerged in an oil bath (R<<h), we assume an isothermal system so that temperature-dependent quantities such as solubility and diffusivity remain constant. With the continuity equation in spherical coordinates, the molar flux of water vapor *N(r)* as a function of radial distance *r* is

$$\frac{1}{r^2}\frac{d}{dr}(r^2 N) = 0 \Rightarrow N(r) = \frac{C_1}{r^2} \tag{S3}$$

where C_1 is a constant of integration that will be evaluated later. Assuming negligible convective transport, Fick's equation can be simplified as

$$N = -D\frac{dc}{dr} \tag{S4}$$

where *D* is the diffusivity of water in oil and *c* is the molar concentration of water. Combining equations (S3) and (S4),

$$\frac{dc}{dr} = -\frac{C_1}{D}\left(\frac{1}{r^2}\right) \tag{S5}$$

Since the diffusion distance varies at any angle (with respect to the horizontal), the radial distance from the droplet center to the oil-air interface is $r = \frac{h}{\sin\phi}$. To facilitate integration, we express the boundary conditions in terms of *R*. We can write $\frac{h}{\sin\phi} = R + \frac{h - R\sin\phi}{\sin\phi}$. Given that $h \gg R\sin\phi$, we can approximate $\frac{h}{\sin\phi} \approx R + \frac{h}{\sin\phi}$. Integrating equation (S5) with boundary conditions $c(R) = c_s$ and $c\left(R + \frac{h}{\sin\phi}\right) = c_\infty$, we obtain

$$\int_{c_s}^{c_\infty} dc = -\frac{C_1}{D}\int_{r=R}^{r=R+\frac{h}{\sin\phi}}\left(\frac{1}{r^2}\right)dr \Rightarrow C_1 = D(c_\infty - c_s)\left(\frac{1}{R} - \frac{1}{R + \frac{h}{\sin\phi}}\right)^{-1} \tag{S6}$$

Combining equations (S3), and (S6), we can write the molar flux as

$$N(r,\phi) = D\left(c_\infty - c_s\right)\left(\frac{1}{R} - \frac{1}{R + \frac{h}{\sin\phi}}\right)^{-1}\left(\frac{1}{r^2}\right) \quad \text{(S7)}$$

Now, we can express the rate of change in droplet volume as the mass flux of water vapor integrated over the droplet surface area A.

$$\frac{dm}{dt} = \int_{surface} M_w N(r,\phi) dA \quad \text{(S8)}$$

The differential surface area d*A* can be written as a function of the differential angle $d\phi$ as

$$dA = (2\pi r\cos\phi)(rd\phi) \quad \text{(S9)}$$

Combining equations (S7), (S8) and (S9) and integrating ϕ from 0 to π/2 (because we consider the case of hemispherical droplet where θ = π/2), we get

$$\frac{dm}{dt} = \int_0^{\frac{\pi}{2}} M_w D\left(c_\infty - c_s\right)\left(\frac{1}{R} - \frac{1}{R + \frac{h}{\sin\phi}}\right)^{-1}\left(\frac{1}{r^2}\right)(2\pi r\cos\phi)(rd\phi) \quad \text{(S10)}$$

$$\frac{dm}{dt} = -(2\pi R)DM_w\left(c_s - c_\infty\right)\left(1 + \frac{R}{2h}\right) \quad \text{(S11)}$$

Note that this is similar to that of Popov[5] for pure droplets directly evaporating in air. By comparison, if we substitute θ = π/2 in the shape factor expression (equation 4 in the main text), we obtain *f(θ)* = 2 (via numerical integration)*, i.e.*

$$f\left(\frac{\pi}{2}\right) = \frac{\sin\left(\frac{\pi}{2}\right)}{1 + \cos\left(\frac{\pi}{2}\right)} + 4\int_0^\infty \frac{1 + \cosh(2(0.5\pi)\varepsilon)}{\sin(2\pi\varepsilon)}\tanh\left[\left(\pi - \frac{\pi}{2}\right)\varepsilon\right]d\varepsilon = 2 \quad \text{(S12)}$$

Furthermore, note that $\left(1 + \frac{R}{2h}\right) \approx 1$ since R<<h. Thus, we incorporate the shape factor *f(θ)* for any contact angle θ as

$$\frac{dm}{dt} = -\pi RDM_w\left(c_s - c_\infty\right)\left(1 + \frac{R}{2h}\right)f(\theta) \quad \text{(S13)}$$

2.1.2. Introduction of the relative humidity (leading to equation 6 in the main text)

The relative humidity *RH* is defined as water vapor concentration divided by the concentration at saturation c_s (in this case, the solubility of water in oil). Thus, we can write

$$\left(c_s - c_\infty\right) = c_s\left(RH_s - RH_\infty\right) \tag{S14}$$

where RH_s and RH_∞ are the relative humidity at the droplet-oil interface (saturated) and oil-air interface, respectively. For pure water droplets, RH_s is always equal to 1. As a result, equation (S13) can be written as

$$\frac{dm}{dt} = -\pi R D M_w c_s\left(RH_s - RH_\infty\right)\left(1 + \frac{R}{2h}\right) f(\theta) \tag{S15}$$

Note that *m* is the mass of the volatile component (in this case, water). Using the definition of density, we can write $m = \rho_w V$ where ρ_w and *V* are the density and volume of pure water respectively. Since ρ_w is constant, $\frac{dm}{dt} = \rho_w \frac{dV}{dt}$. We can then combine the constant terms as $K = \frac{DM_w c_s}{\rho_w}$. Thus, equation (S15) can be re-written as

$$\frac{dV}{dt} = -\pi R K\left(RH_s - RH_\infty\right)\left(1 + \frac{R}{2h}\right) f(\theta) \tag{S16}$$

Note that this is valid for isolated droplets (i.e., no neighbors).

2.2 Considering the changes in droplet density as water evaporates

2.2.1. Determination of the density of salt solution

Note that we defined *V* as the volume of pure water (the volatile component) and *R* as the radius of the entire droplet. However, the total volume of the droplet V_d is a function of the volume occupied by both water and salt ions. To relate the volume of pure water *V* to the droplet volume V_d, we employ experimental data on the solution density change as a function of NaCl supersaturation ratio ($S = c/c_{eq}$, where c is the concentration of salt in the solution and c_{eq} its solubility) as shown in **Figure S2**. We then use a simple linear function with b_1 (slope) as the dimensionless coefficient of density increase relating the density of pure water ρ_w and the density ρ at any *S*.

$$\rho = \rho_w(1 + b_1 S) \tag{S17}$$

2.2.2. Determination of droplet radius

Given that the droplet mass is the sum of water mass and NaCl mass ($m_d = m_w + m_{NaCl}$), we can write

$$\frac{m_w + m_{\text{NaCl}}}{V_d} = \frac{m_w}{V}(1 + b_1 S) \Longrightarrow \frac{1 + \left(\frac{m_{\text{NaCl}}}{m_w}\right)}{V_d} = \frac{1 + b_1 S}{V} \quad \text{(S18)}$$

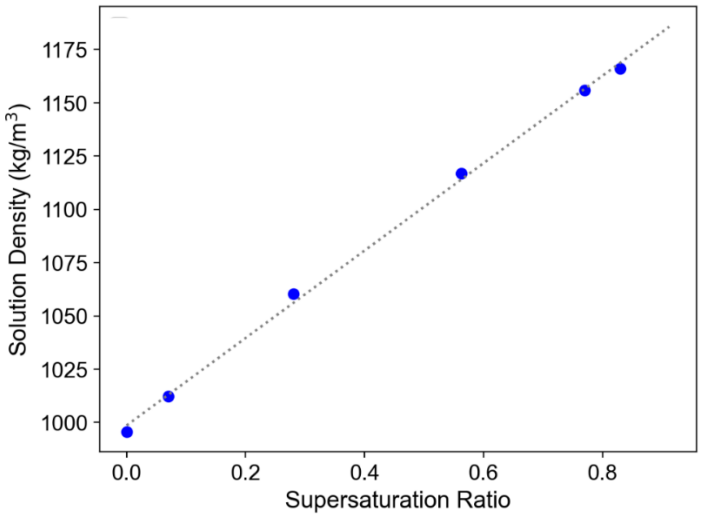

Figure S2. Variation of aqueous NaCl density as a function of supersaturation ratio.[6] The regression line is $y = 998(1+0.205x)$ with $R^2 = 0.9984$.

We can express m_{NaCl}/m_w in terms of S using the solubility of NaCl in water c_{eq} (in mol/kg water) and NaCl molar mass M_{NaCl} (kg/mol)

$$\frac{m_{\text{NaCl}}}{m_w} = c_{eq} M_{\text{NaCl}} S \quad \text{(S19)}$$

Thus, the droplet volume V_d is related to the volume of pure water V as

$$V_d = \left(\frac{1 + c_{eq} M_{\text{NaCl}} S}{1 + b_1 S}\right) V \quad \text{(S20)}$$

Observe that for pure droplet (S=0), $V_d = V$. We can now express the droplet radius R in terms of V using the equation for the volume of spherical cap along with the density changes.

$$R = \left(\frac{V_d}{\pi g(\theta)}\right)^{\frac{1}{3}} = \left[\frac{V\left(1 + c_{eq} M_{\text{NaCl}} S\right)}{(1 + b_1 S)\pi \cdot g(\theta)}\right]^{\frac{1}{3}} \text{ with } g(\theta) = \frac{\sin\theta\,(\cos\theta + 2)}{3(1 + \cos\theta)^2} \quad \text{(S21)}$$

This expression for R will be used in equation S16.

2.3. Dependence of water activity on solute concentration

To account for the change in water activity due to the presence of salt, we express the decrease in water activity as a linear function with slope b_2 fitted from experimental data of An et al, as shown in **Figure S3**.[7]

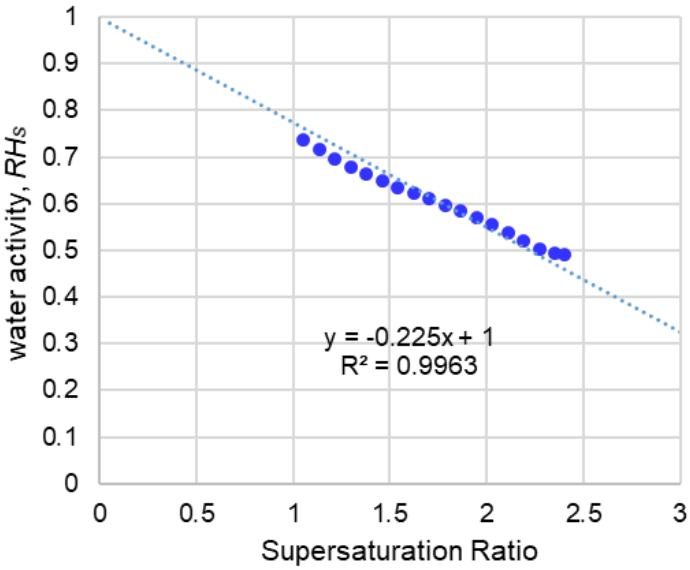

Figure S3. Variation of water activity (numerically equal to the equilibrium relative humidity, RH_s) as a function of supersaturation ratio. The data were taken from Table 6 of An et al.[7]

Thus, in equation (S28) the saturation relative humidity RH_s is expressed as

$$RH_s = 1 - b_2 S \tag{S22}$$

where b_2 is the coefficient of vapor pressure lowering fitted from experimental data of An et al.[7] Since the total mass of the salt is constant, we can write $S_0 V_0 = SV$ so all equations containing S can be expressed in terms of V.

2.4. Considering the presence of neighboring droplet

We adapt the result of Masoud *et al.*[8] who derived analytical expressions to describe the collective evaporation of multiple droplets applicable for any arbitrary configuration (1D or 2D array). Accordingly, if there are N droplets in the system, then the evaporation rate of each droplet J_n is

$$\frac{J_n}{\hat{J}_n} = 1 - \sum_{m=1}^{N} \hat{\Phi}_{r_m} \frac{J_m}{\hat{J}_n} \tag{S23}$$

where $\hat{J}_n$ is the rate of an equivalent isolated droplet, $\widehat{\Phi}_{r_m}$ and J_m are the normalized vapor concentration and evaporation rate at the location of m^{th} droplet respectively. The expression $\widehat{\Phi}_{r_m}$ is a function of separation distance, which can be written as

$$\widehat{\Phi}_{r_m} = 4A\frac{R}{\tilde{r}} + (A - 4B)(\tilde{r}^2 - 3\tilde{z}^2)\frac{R^3}{\tilde{r}^5} + O\left[\left(\frac{R}{\tilde{r}}\right)^5\right] \tag{S24}$$

where

$$A = \int_0^\infty \left\{1 + \frac{\cosh[(2\pi - \theta)\tau]}{\cosh(\theta\tau)}\right\}^{-1} d\tau \quad , \quad B = \int_0^\infty \left\{1 + \frac{\cosh[(2\pi - \theta)\tau]}{\cosh(\theta\tau)}\right\}^{-1} \tau^2 d\tau \tag{S25}$$

in which $\tilde{r} = |r - r_c|$ and r_c is the location of the center of droplet's contact area, $\tilde{z}$ is the z-coordinate at $\tilde{r}$, θ is the contact angle, and τ is an arbitrary constant of integration.

Note that equation (S23) leads to a system of *N* linear equations which gives evaporation rates for each droplet. In a special case of long 1-D array of monodisperse microdroplets (*N* > 60), each one tends to evaporate at the same rate (i.e. $J_n \approx J_m$). With this assumption, we can approximate equation (S23) to a single equation as

$$\frac{J_n}{\hat{J}_n} = \left(1 + \sum_{m=1}^{N} \widehat{\Phi}_{r_m}\right)^{-1} \tag{S26}$$

To check how the approximation in equation (S*26*) deviates from the full equation of Masoud et al[8] (S*23*), we compare the predictions of both equations as a function of number of droplets (1D-case). We see that at large number of droplets, the two models converge (**Figure S4**).

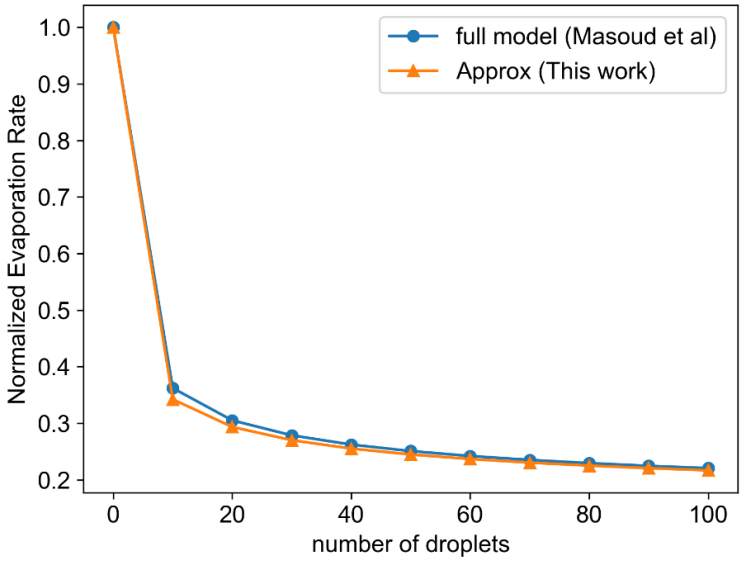

Figure S4. Comparison of the full model (Masoud et al, equation S23) for the middle droplet against our approximation (equation S26) considering θ =π/2 and L/R_0 = 2.5.

Furthermore, the normalized evaporate rate $J_n/\hat{J}_n$ is related to the effective relative humidity as

$$\frac{J_n}{\hat{J}_n} = \frac{RH_s - RH_{eff}}{RH_s - RH_\infty} \tag{S27}$$

Thus, to describe the evaporation of microdroplet arrays, we replace RH_∞ with RH_{eff} in equation (S16) which gives

$$\frac{dV}{dt} = -\pi RK\left(RH_s - RH_{eff}\right)\left(1 + \frac{R}{2h}\right)f(\theta) \tag{S28}$$

3. Models for Contact Line Behavior

The contact line behavior (how the contact radius and contact angle evolve with time) generally depends on the nature of the surface where the sessile microdroplet is situated. In the extreme case of perfectly smooth chemically homogeneous surface, the droplet maintains an equilibrium contact angle, and this is referred to as constant contact angle (CCA) mode. Consequently, the volume decreases due to the continuous decrease in contact radius.[2]

In practice, the droplet will be pinned due to surface roughness so the radius remains constant at some point. In the extreme case where the droplet remains pinned throughout its lifetime, we refer to this as the constant contact radius (CCR) mode. In this mode, the volume decreases due to the continuous decrease in contact angle. As experimental studies suggest,[9] real droplets evaporate in some mixture of CCR and CCA modes. One common observation is the occurrence of CCR mode at the beginning and once the contact angle decreases to a value less than the receding contact angle θ_r, it switches to CCA mode. This combination is known as the stick-slide (SS) mode.[9] In this work, we consider all three cases (CCA, CCR, and SS models) in analyzing the experimental data.

Mathematically, we can then incorporate the contact-line behavior by modeling the behavior of the contact angle θ.

3.1. For constant contact angle mode (CCA)

For constant contact angle mode (CCA), the change in contact angle with time is simply,

$$\frac{d\theta}{dt} = 0 \tag{S29}$$

3.2. For constant contact radius mode (CCR)

For constant contact radius mode (CCR), the change in contact angle with time can be obtained by taking the derivative of V = $f(\theta,R)$ where R is constant (see **Figure S1**)

$$V = \pi R^3 g(\theta) \Rightarrow \frac{dV}{dt} = \pi R^3 \frac{d}{dt}[g(\theta)] \text{ with } g(\theta) = \frac{\sin\theta\,(\cos\theta + 2)}{3(1+\cos\theta)^2} \tag{S30}$$

$$\frac{d}{dt}[g(\theta)] = \frac{d}{dt}\left(\frac{\sin\theta\,(\cos\theta + 2)}{3(1+\cos\theta)^2}\right) = \frac{1}{(1+\cos\theta)^2}\frac{d\theta}{dt} \tag{S31}$$

Combining equations (S30) and (S31), we can obtain the change in contact angle as

$$\frac{d\theta}{dt} = \frac{1}{V}\frac{dV}{dt}(1+\cos\theta)^2 g(\theta) \tag{S32}$$

3.3. For stick-slide mode (SS)

For stick-slide mode (SS), the evaporation follows CCR mode, that is, the initial contact angle θ_0 decreases until it reaches the receding contact angle θ_r where it suddenly shifts to the CCA model[2]. Then, the full SS model can be written as

$$\frac{d\theta}{dt} = \begin{cases} \frac{1}{V}\frac{dV}{dt}(1+\cos\theta)^2 g(\theta) & \text{for } \theta_r \le \theta \le \theta_0 \\ 0 & \text{for } 0 < \theta < \theta_r \end{cases} \quad \text{(S33)}$$

4. Parameters and properties

4.1 Properties of products

***Table S2**. Properties of products*

Product	Supplier	Properties
Sodium chloride, NaCl	R.P Normapur ®	Purity = 99.5% Refractive index = 1.5442
Polymethylmethacrylate, PMMA	ALLRESIST GmbH	Molecular weight= 950,000 g/mol Refractive index = 1.395
Polydimethylsiloxane, PDMS oil	Alfa Aesar	Molecular weight = 1250 g/mol Viscosity = 10 cSt Refractive index = 1.3990
Ultrapure water	via Milli-Q Purifier	resistivity = 18.2 MΩ·cm TOC value < 5 ppb

4.2 Determination of solubility of water in PDMS

We measured the solubility of water in PDMS oil (10 cSt) using Karl-Fischer Titrator C20 (Mettler Toledo). We mixed the oil and water (Vortex mixer, for 5 min) then the system is equilibrated for 2 days. Around 0.5 g sample of the oil was taken for Karl-Fischer titration.

Table S1 Solubility of PDMS oil (10 cSt) in water at 25°C measured using Karl-Fischer technique.

	ppm	mol/m^3
Trial 1	164.8	8.560
Trial 2	145.0	7.532
Trial 3	173.7	9.023
Trial 4	190.8	9.911
average	168.6	8.76 (±1)

4.3 Determination of diffusivity of water in PDMS

We measured the diffusivity of water in PDMS from the evaporation of isolated pure water sessile droplet with V_0=1.6 nL at *RH*=0.34 (3 replicates). The value is calculated from the slope of $(V/V_0)^{2/3}$ vs time based on the analytical solution of Picknett and Bexon[9] (**Figure S5**)

$$V^{2/3} = V_0^{2/3} - \alpha t \qquad \text{(S34)}$$

where V is the volume at any time t, V_0 is the initial volume, t is time, and α is given by

$$\alpha = \frac{2Cf}{3\beta^{\frac{1}{3}}} \quad \text{(S34a)}$$

where

$$C = 2\pi D \left(\frac{3}{\pi}\right)^{\frac{1}{3}} \left(\frac{Mc_s \Delta RH}{\rho}\right) \quad \text{(S34b)}$$

$$f = 0.00008957 + 0.6333\theta + 0.116\theta^2 - 0.08878\theta^3 + 0.01033\theta^4,\ \theta > 10^o \quad \text{(S34c)}$$

$$\beta = (1 - \cos\theta)^2(2 + \cos\theta) \quad \text{(S34d)}$$

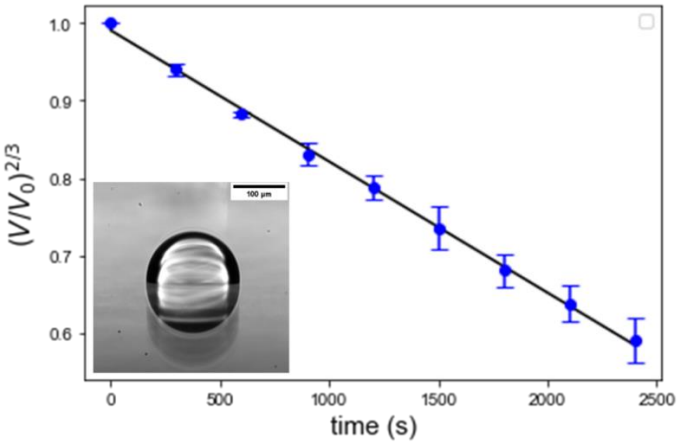

Figure S5. Plot of $(V/V_0)^{2/3}$ vs time. From the slope, the diffusivity of water in PDMS oil can be determined using equation S34, from which we obtained $D = 6.74 \times 10^{-9}$ m^2s^{-1}.

The complete list of numerical values used in the modeling is tabulated in Table S3.

Table S3 Numerical values used as input in the CCA evaporation model of saline droplets

Quantity	Symbol	Value	Unit
solubility of water in PDMS oil	c_s	8.76	mol/m^3
diffusivity of water in PDMS oil	D	6.74×10^{-9}	m^2s^{-1}
coefficient of density change[6]	b_1	0.205	-
coefficient of water activity lowering[7]	b_2	0.225	-
solubility of NaCl in water[10]	c_{eq}	6.14	mol/kg
molar mass of NaCl	M_{NaCl}	0.0584	kg/mol
diffusivity of NaCl in water[11]	D_i	1.47×10^{-9}	m^2/s
density of pure water[6]	ρ_w	997	kg/m^3

5. Measurements in Saline Microdroplets

5.1. Homogeneity of Droplet Concentration

In the equations (S31), we approximate that the temperature and concentration are essentially homogeneous. The homogeneity of droplet composition is characterized by Peclet number *Pe,* which is the ratio of convective mass transfer to diffusive mass transfer[12]. It is expressed as[13]

$$Pe = \frac{2R\kappa}{D_i} \tag{S35}$$

Where κ is the evaporation flux (volume loss *dV/dt* per unit area *A*), *R* is the droplet radius and D_i is the diffusion coefficient of the solute in the droplet. If Pe < 1, the diffusion rate of the solute is fast enough to avoid a considerable enrichment at the receding surface and thus the system maintains a homogeneous composition. In our experiments, *Pe* is in the order of 10^{-4} (**Figure S6**), thus we can treat the microdroplets as homogeneous solution (with negligible concentration gradient).

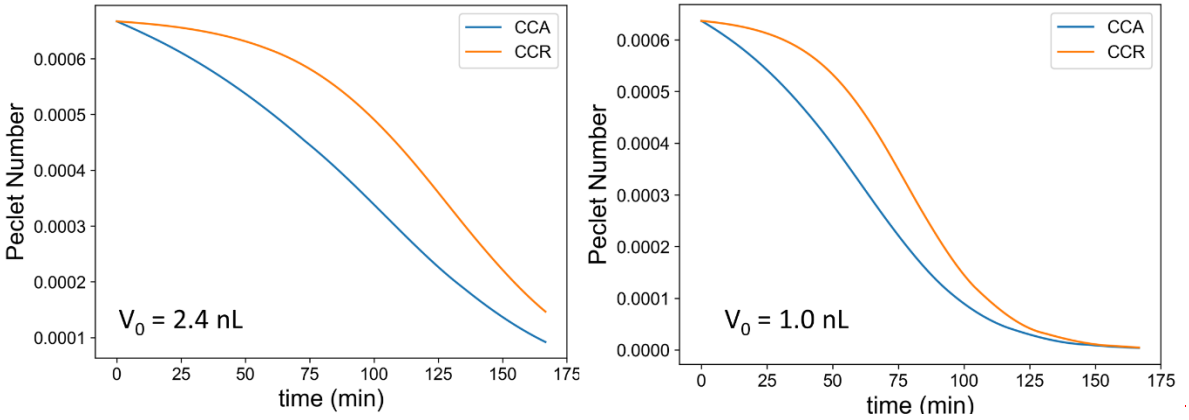

Figure S6. Evolution of Peclet number for CCA and CCR models corresponding to the experimental condition described in Figure 5 of the main text. (If Peclet number << 1, the microdroplet is considered to have homogeneous composition)

5.2 Characteristic Time Point Measurement using Axial Microscope

To validate our models for saline droplets, we generated arrays of sessile saline microdroplets on PMMA-coated glass immersed in a thin film of PDMS oil using the method described by Grossier et al.[14] (**Figure S7**)

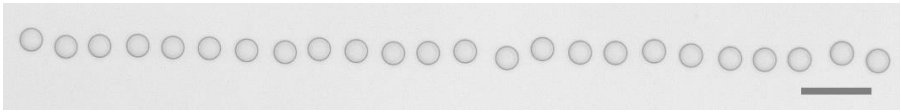

Figure S7. Image of a typical microdroplet array (scale bar = 200 µm)

On 190 independent microdroplets, we measured three characteristic times namely the saturation time (time when the microdroplet is saturated, S=1), the matching time (time when the refractive index of the droplet matches that of the PDMS oil, S = 1.395) and the nucleation time. Our approach is to use image analysis to determine these three points as demonstrated in our previous work.[15] Briefly, the standard deviation of the gray-level pixel histogram (denoted as σ, a function of refractive index difference) corresponding to the region surrounding the microdroplet image (axial view) is used as an indicator of droplet concentration.

6. Effect of Relative Humidity on the Predicted Supersaturation at Nucleation

To investigate the impact of relative humidity on the predicted supersaturation of microdroplets, we performed two sets of experiments at identical configuration (V_0 = 55 pL, S_0 = 0.70, L_1/R_0=5.6, L_2/R_0 =32) but at different hygrometric conditions, i.e. dry conditions (RH = 0.10) and ambient conditions (RH = 0.35). This is done by exploiting the cycling method developed in Ref.[16]

The results are plotted in **Figure S8**. The constant dV/dt model clearly overestimates S_n and the error becomes particularly important at higher RH. Interestingly, our model correctly predicts the nucleation of NaCl*(aq)* at around S=1.6 regardless of hygrometric conditions.

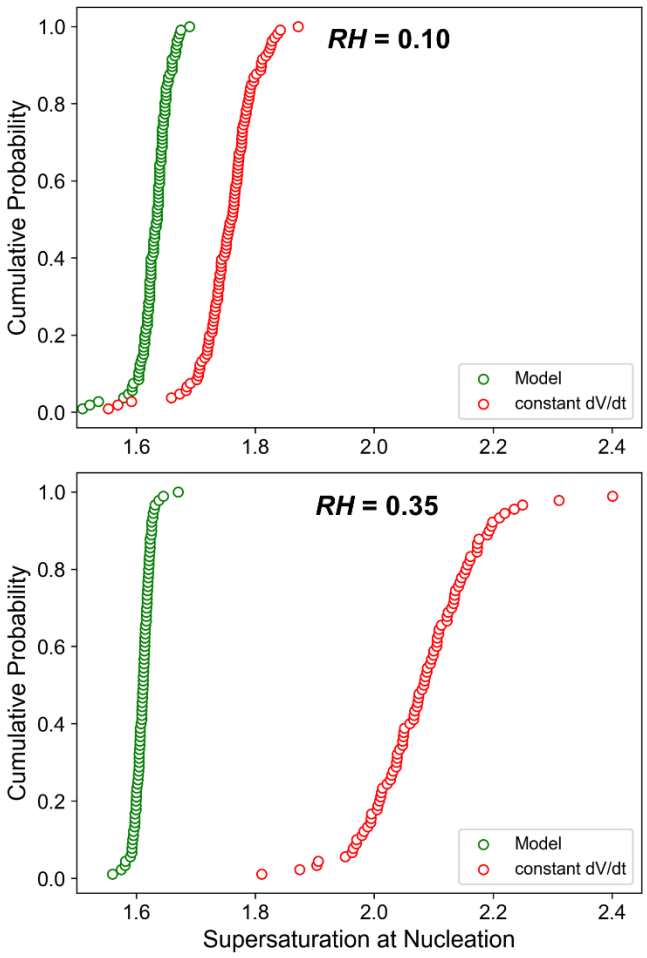

Figure S8. Cumulative probability distribution of supersaturation at nucleation S_n for microdroplets at identical experimental configuration (*V_0 = 55 pL, S_0 = 0.70, L_1/R_0=5.6, L_2/R_0 =32)* but at different hygrometric conditions.

REFERENCES

1. Yu, Y.-S.; Yang, Z.; Zhao, Y.-P., Role of Vertical Component of Surface Tension of the Droplet on the Elastic Deformation of PDMS Membrane. *J. Adhes. Sci. Technol.* **2008,** *22* (7), 687-698.
2. Stauber, J. M.; Wilson, S. K.; Duffy, B. R.; Sefiane, K., On the lifetimes of evaporating droplets with related initial and receding contact angles. *Physics of Fluids* **2015,** *27* (12), 122101.
3. Stauber, J. M.; Wilson, S. K.; Duffy, B. R.; Sefiane, K., Evaporation of droplets on strongly hydrophobic substrates. *Langmuir* **2015,** *31*, 3653.
4. Nguyen, T. A. H.; Nguyen, A. V.; Hampton, M. A.; Xu, Z. P.; Huang, L.; Rudolph, V., Theoretical and experimental analysis of droplet evaporation on solid surfaces. *Chem. Eng. Sci.* **2012,** *69*, 522.
5. Popov, Y. O., Evaporative deposition patterns: Spatial dimensions of the deposit. *Physical Review E* **2005,** *71* (3), 036313.
6. Don, W. G.; Robert, H. P., *Perry's Chemical Engineers' Handbook, Eighth Edition*. 8th ed. / ed.; McGraw-Hill Education: New York, 2008.
7. An, D. T.; Teng, T. T.; Sangster, J. M., Vapour pressures of CaCl2–NaCl–H2O and MgCl2–NaCl–H2O at 25 °C. Prediction of the water activity of supersaturated NaCl solutions. *Can. J. Chem.* **1978,** *56* (14), 1853-1855.
8. Masoud, H.; Howell, P. D.; Stone, H. A., Evaporation of multiple droplets. *J. Fluid Mech.* **2021,** *927*, R4.
9. Picknett, R. G.; Bexon, R., The evaporation of sessile or pendant drops in still air. *J. Colloid Interface Sci.* **1977,** *61*, 336.
10. Benavides, A. L.; Aragones, J. L.; Vega, C., Consensus on the solubility of NaCl in water from computer simulations using the chemical potential route. *The Journal of Chemical Physics* **2016,** *144* (12), 124504.
11. Vitagliano, V.; Lyons, P. A., Diffusion Coefficients for Aqueous Solutions of Sodium Chloride and Barium Chloride. *JACS* **1956,** *78* (8), 1549-1552.
12. Boel, E.; Koekoekx, R.; Dedroog, S.; Babkin, I.; Vetrano, M. R.; Clasen, C.; Van den Mooter, G., Unraveling Particle Formation: From Single Droplet Drying to Spray Drying and Electrospraying. *Pharmaceutics* **2020,** *12* (7), 625.
13. Gregson, F. K. A.; Robinson, J. F.; Miles, R. E. H.; Royall, C. P.; Reid, J. P., Drying Kinetics of Salt Solution Droplets: Water Evaporation Rates and Crystallization. *The Journal of Physical Chemistry B* **2019,** *123* (1), 266-276.
14. Grossier, R.; Hammadi, Z.; Morin, R.; Magnaldo, A.; Veesler, S., Generating nanoliter to femtoliter microdroplets with ease. *Appl. Phys. Lett.* **2011,** *98* (9), 091916.
15. Grossier, R.; Tishkova, V.; Morin, R.; Veesler, S., A parameter to probe microdroplet dynamics and crystal nucleation. *AIP Advances* **2018,** *8* (7), 075324.
16. Cedeno, R.; Grossier, R.; Lagaize, M.; Nerini, D.; Candoni, N.; Flood, A.; Veesler, S., Nucleation in sessile saline microdroplets: induction time measurement via deliquescence–recrystallization cycling. *Faraday Discuss.* **2022,** *235* (0), 183-197.